



Research Paper

Comprehensive efficiency analysis of air-cooled vs water-cooled electric motor for unmanned aerial vehicle

Min Chang^a, Bingzhu Lai^b, Hui Wang^{b,*}, Junqiang Bai^{a,b}, Zhaoyong Mao^a^a Unmanned System Research Institute, Northwestern Polytechnical University, Xi'an, Shaanxi 710072, China^b School of Aeronautics, Northwestern Polytechnical University, Xi'an, Shaanxi 710072, China

ARTICLE INFO

Keywords:

Electric unmanned aerial vehicle
Cooling method
Thermal performance
Efficiency improvement

ABSTRACT

The efficiency of an electric motor for an unmanned aerial vehicle can reduce when its temperature exceeds the working temperature. In this paper, air- and water-cooling methods for electric motors in unmanned aerial vehicles are proposed and comprehensively compared. The effects of fan speed, water flow speed, and convection heat transfer coefficient on the outer surface of the electric motor on the cooling capacity of the electric motor are discussed. A comprehensive performance evaluation factor for the cooling method of the motor is proposed. Results show that when the fan speed increased from 800 to 2000 rpm, the cooling efficiency increased by 27.78% for the air-cooled motor, whereas when the inlet flow rate of cooling water increased from 0.1 to 0.9 m/s, the cooling efficiency increased by 67.47% for the water-cooled motor. The comprehensive performance of the water-cooled motor reached the highest level with a velocity of 0.7 m/s. The convection heat transfer coefficient increased from 5 to 25 W/(m²·K), and the cooling efficiency increased by 22.93% and only 2.77% for the air- and water-cooled motors, respectively. These findings can provide guidance for designing highly efficient electric motor cooling equipment for unmanned aerial vehicles.

1. Introduction

Electric propulsion technology has a wide range of applications in electric vehicles [1,2], high-speed electric trains [3], solar-powered unmanned aerial vehicles (UAVs) [4,5], and electric commercial aircraft [6]. An electric motor is an indispensable component of electric propulsion systems. In an environment with good heat dissipation, the power density of the electric motor can reach a high level. When the temperature of the electric motor exceeds the working temperature for a long time, it can cause adverse phenomena such as aging of materials in the electric motor, demagnetization of permanent magnets, and geometric deformation [7,8], which significantly reduce the reliability, service life, and efficiency of the electric motor. Therefore, controlling the temperature is important to improving the efficiency of the electric motor for UAVs under different working conditions.

The air cooling method removes heat by introducing air flowing into the electric motor. For example, Kim et al. [9] eliminated the influence of stagnant flow by installing air-gap fans on both sides of a motor. They observed that using an air-gap fan could increase the cooling performance by 55%, and the air-gap fan on the rear side of the motor had higher efficiency than that of the air-gap fan on the front side. Their

study considered the air speed at the inlet boundary as a constant value, and the effect of the fan speed on the air inlet speed was ignored. Kang et al. [10] proposed a self-ventilating cooling structure for an electric motor. They observed that the new cooling structure could reduce the temperature of permanent magnets by 7%. The fan structure was not considered in their model, and the inlet velocity was given a constant value. Hyeon et al. [11] designed a cooling system with a flow guide to enhance the cooling efficiency. They observed that the flow guide increased the cooling effect by 28%. The fan structure was not described in their model, and the magnitude of the inlet velocity was directly set. Galloni et al. [12] evaluated the performances of different fan shapes in an air-cooled motor. They observed that the ratio of the impeller's height to its diameter affected the airflow through the motor. Although they considered the structure of the fan, the specific structure of other parts of the motor was ignored, and the influence of the overall structure of the motor on the flow characteristics was not considered. Most previous studies simplified fans without considering different fan speeds. Although a few studies have considered the fan, the other parts of the motor have been ignored. The motor fan and other structures have an interactive relationship; therefore, the entire motor should be modeled during the research process to obtain an accurate simulation result.

The liquid cooling of a motor uses liquid to flow in a fixed area of the

* Corresponding author.

E-mail address: wanghui2018@nwpu.edu.cn (H. Wang).

Nomenclature	
c_p	Constant pressure specific heat capacity [J/(kg·K)]
G	Turbulent kinetic energy caused by the average velocity gradient (W/m^3)
h	Convection heat transfer coefficient (CHTC) [$\text{W}/(\text{m}^2 \cdot \text{K})$]
k	Turbulent kinetic energy (J)
K	Thermal Conductivity [$\text{W}/(\text{m} \cdot \text{K})$]
M	Motor weight (kg)
n	Gradient direction
P	Pressure of fluid (Pa)
Pr	Prandtl number
q	Calorific value per unit volume (W/m^3)
T	Temperature (K)
u	Velocity in x direction (m/s)
v	Velocity in y direction (m/s)
w	Velocity in z direction (m/s)
x	x direction
y	y direction
z	z direction
<i>Greek symbols</i>	
ε	Turbulent kinetic energy dissipation rate
ρ	Density (kg/m^3)
μ	Dynamic viscosity (Pa·s)
<i>Subscript</i>	
am	Ambient
$cool$	Cooling structure
eff	Effective value
f	Fluid
ori	Original structure
out	Outer surface
s	Solid
$shell$	Motor shell
t	Turbulence

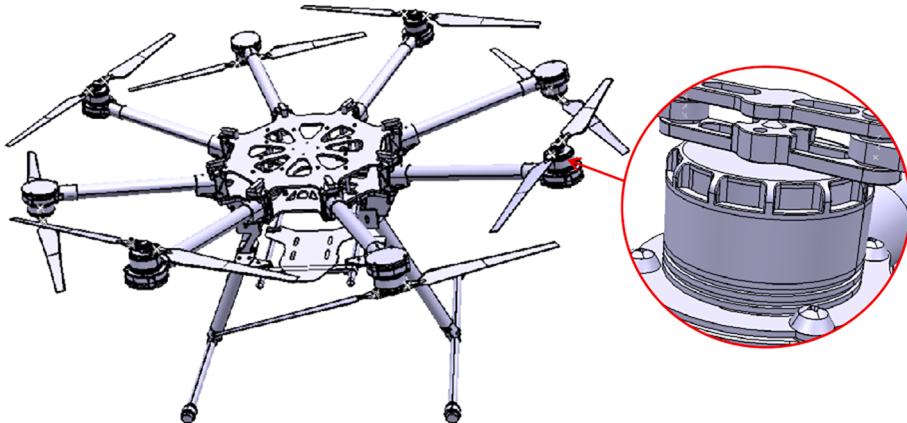


Fig. 1. Schematic diagram of UAV structure.

motor for heat exchange. For example, Pei et al. [13] designed a water-cooling structure with a primary water-cooling plate for motor cooling and studied the effect of heat dissipation on the structure. They observed that the designed water-cooling structure significantly reduced the temperature increase and prevented the motor from burning out. They only considered the structure of the water-cooled plate and did not consider the structure of the motor, including the stator core, windings, and permanent magnets. Chiu et al. [14] evaluated the cooling performance of a reluctance motor. They observed that the temperature increase of the windings of the motor could be reduced to 42% after cooling using liquid water. Although they modeled the motor winding and stator core, they did not consider the influence of the rotation function on the performance of the motor. Han et al. [15] conducted an integrated design of a 30 kW motor water-cooled radiator and investigated the cooling performance of three radiator configurations. They observed that the serpentine channel exhibited good cooling performance and temperature uniformity. They did not consider the entire motor structure and only modeled the designed heat sink. Ge et al. [16] calculated the heat dissipation effect on a motor. They observed that the cooling performance of the circumferential helical coolant channel was better than that of an axial S-shaped flow channel. They directly simplified the components of the motor into temperature nodes without considering the actual structure of the motor. Most scholars have simplified the model and ignored the influence of the motor structure on

the heat dissipation performance; therefore, they neglected the coupling effect of the water-cooling device and motor.

As reviewed above, the electric motor model has been simplified to some extent in previous studies, and the interaction between the cooling device and motor has been ignored. In this paper, the motor model is built in detail, the interaction between the cooling device and the motor is considered in the simulation. The heating capacity of the windings in the motor was determined through experiments, and the temperature distribution of the UAV motor under different cooling modes (including air- and water-cooling methods) was simulated. In the air-cooled motor, the motor mainly cools the heat source by drawing in the cold air of the external low temperature through the fan. In the water-cooled motor, the motor cools the heat source by introducing cooling water. In this paper, the influence of fan speed and convection heat transfer coefficient (CHTC) on the cooling capacity of air-cooled motor, and the influence of cooling water speed and CHTC on the cooling capacity of water-cooled motor are considered. Finally, the cooling capacity of the motor under different cooling modes is comprehensively evaluated. The research in this paper can directly provide some guidance for the motor design on UAV in different occasions.

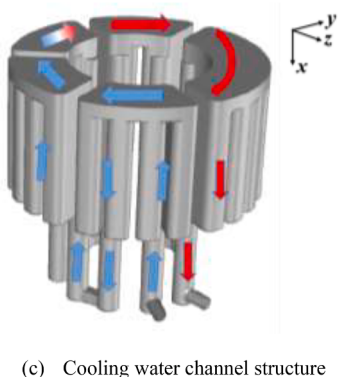
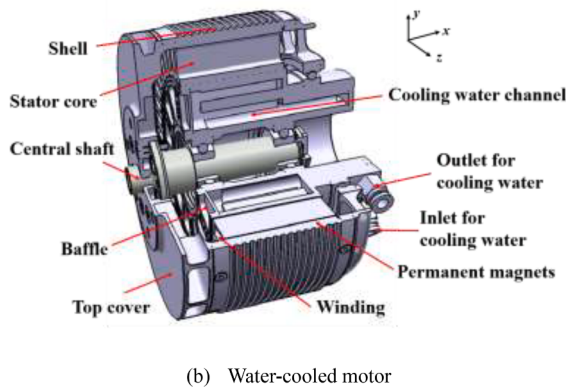
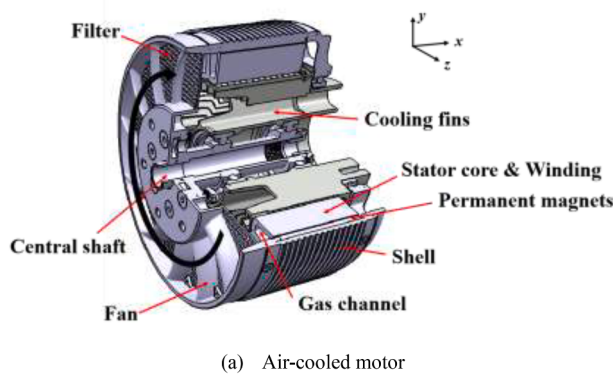


Fig. 2. Schematic of the outer rotor motor model.

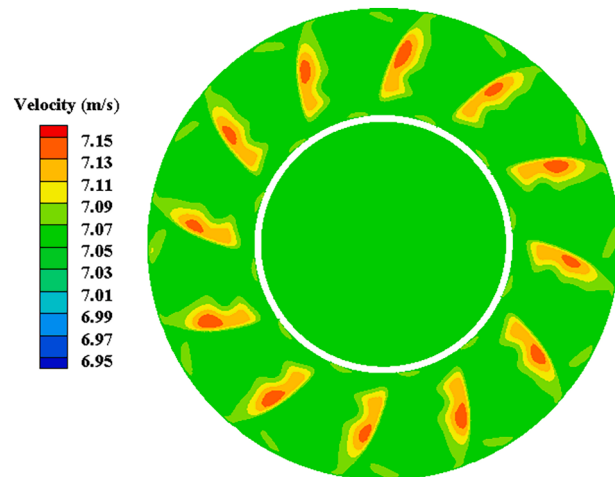


Fig. 3. Speed distribution of the section of the fan (800 rpm).

2. Problem Description

2.1. Geometrical Model

The structure of UAV mainly includes chassis, battery, motor, propeller, fuselage main board, landing frame and connecting arm. Fig. 1 shows a typical structure diagram of UAV, and the motor structure is partially enlarged. During the flight of the UAV, the motor on the UAV is powered by the power supply, and the motor converts the electric energy into kinetic energy to drive the rotor on the UAV to rotate. Electronic energy is converted into heat energy, which results in an increase in the temperature of the motor. When the temperature of the motor exceeds the working temperature, the working efficiency of the electric motor and the rotational speed of the rotatory wing decrease [17].

Permanent magnet synchronous motors are widely used in UAVs because of their high efficiency and power density [18]. To dissipate heat for the electric motor in a UAV, air- and water-cooled motors are designed based on a permanent magnet synchronous motor. Fig. 2 (a) and (b) shows the physical models of the air- and water-cooled motors, respectively. Air-cooled motors are primarily composed of the fan, filter, central shaft, shell, stator core, winding, permanent magnets, and cooling fins. The shell and permanent magnet parts constitute the rotor of the motor. The airflow path in the air-cooled motor is the gap between the stator core and winding. In the air-cooled motor, the rotating parts include the fan, filter, central shaft, shell and permanent magnets, which are driven by the power supply to rotate clockwise. The suction generated by the rotation of the fan sucks the surrounding cold air into the motor. After entering the motor, the cold air flows through the gap between the stator core and winding and flows in the axial direction to cool the stator core and winding. Subsequently, the air flows out from the bottom of the motor.

The structure of the water-cooled motor is composed of a top cover, central shaft, baffle, shell, stator core, winding, cooling-water inlet, cooling-water outlet, and permanent magnets. Similar to the air-cooled motor, the rotating parts of the water-cooled motor include the top cover, the central shaft, shell and permanent magnets. In the water-cooled motor, the circulation path of the cooling water is located between the stator core and central shaft, and the cooling water inlet and outlet boundaries are located at the lower part of the motor. The shape and flow direction of the cooling-water channel are shown in Fig. 2 (c). During the operation of the water-cooled motor, the cooling water flows into the cooling channel of the motor at a certain speed and temperature. After cooling the motor through convection heat exchange, it is discharged from the outlet boundaries.

Whether it is air- or water-cooled, the lower part of the motor is

Table 1
Structural parameters for the air-cooled motor and the water-cooled motors.

Parameter	Air-cooled motor	Water-cooled motor
Model height (m)	1.18×10^{-1}	1.25×10^{-1}
Fan height (m)	1.3×10^{-2}	–
Fan outer diameter (m)	1.68×10^{-1}	–
Fan inner diameter (m)	7.8×10^{-2}	–
Top cover height (m)	–	1.79×10^{-2}
Cooling water inlet and outlet diameters (m)	–	6.2×10^{-3}
Stator outer diameter (m)	1.56×10^{-1}	1.4×10^{-1}
Stator inner diameter (m)	1.02×10^{-1}	1.02×10^{-1}
Rotor outer diameter (m)	1.684×10^{-1}	1.524×10^{-1}
Rotor inner diameter (m)	1.571×10^{-1}	1.411×10^{-1}
Central axis diameter (m)	4.2×10^{-2}	4.2×10^{-2}
Permanent magnet thickness (m)	3.2×10^{-3}	3.2×10^{-3}

Table 2

Calorific value per unit volume under different loads.

Working load (kg)	0	20	40	60
q (W/m ³)	624,312	697,317	1,334,216	1,838,125

Table 3

Boundary conditions of the air-cooled motor.

Boundary condition	Value
Ambient temperature (K)	295
Ambient pressure (Pa)	101,325
Fan inlet temperature (K)	295
Speed of the fan (rpm)	800/1200/1600/2000
Shell convection heat transfer coefficient (W/(m ² ·K))	5/10/15/20/25
Outlet pressure (Pa)	101,325

connected to the static parts. Permanent magnets are attached to the surface of the shell to generate a magnetic field. The winding is wound around the stator teeth, and the motor rotates if a direct current is adopted. During motor operation, the main heating components are the stator core and winding. The structural parameters of the air- and water-cooled motors are listed in [Table 1](#).

The parameters in [Table 1](#) indicate that the diameter of the air-cooled motor is slightly larger than that of the water-cooled motor. This is because the cooling water channel in the water-cooled motor is the area between the stator core and central shaft. However, air passage in air-cooled motor is gap between the winding and stator core. Therefore, in order to ensure that there is enough space in the air-cooled motor as the gas flow channel, the diameter of the stator core of the air-cooled motor must be appropriately expanded. In this way, it can ensure that the volume of air cooled motor winding and water-cooled motor winding is the same, so as to ensure that the heat source power is consistent.

2.2. Mathematical Modeling

The problem has been partially simplified: (1) air is considered an ideal gas and (2) the radiant heat effect is ignored because of low temperature. At the same time, because the motor speed is low, the change of air density is insignificant. As shown in [Fig. 3](#), the air flow rate in the motor is preliminarily calculated, and the speed section at the fan is shown when the motor speed is 800 rpm. It can be seen that the maximum air velocity is about 7.15 m/s, and the corresponding Mach number is 0.02 (the local sound velocity is 344.28 m/s). The value of Mach number is far less than 0.2, so the air compressibility can be ignored [[19,20](#)]. The incompressible solution method can improve the simulation efficiency and reduce the simulation cost while ensuring the accuracy of the calculation results.

The three conservation laws for mass, momentum, and energy conservation should be satisfied. In a steady-state process, the mathematical forms for these three conservation laws are expressed as [[21](#)].

$$\left\{ \begin{array}{l} \text{mass :} \\ \frac{\partial u}{\partial x} + \frac{\partial v}{\partial y} + \frac{\partial w}{\partial z} = 0 \\ \text{momentum :} \\ \rho_f \left(u \frac{\partial u}{\partial x} + v \frac{\partial u}{\partial y} + w \frac{\partial u}{\partial z} \right) = - \frac{\partial P}{\partial x} + \mu_{eff} \left(\frac{\partial^2 u}{\partial x^2} + \frac{\partial^2 u}{\partial y^2} + \frac{\partial^2 u}{\partial z^2} \right) \\ \rho_f \left(u \frac{\partial v}{\partial x} + v \frac{\partial v}{\partial y} + w \frac{\partial v}{\partial z} \right) = - \frac{\partial P}{\partial y} + \mu_{eff} \left(\frac{\partial^2 v}{\partial x^2} + \frac{\partial^2 v}{\partial y^2} + \frac{\partial^2 v}{\partial z^2} \right) \\ \rho_f \left(u \frac{\partial w}{\partial x} + v \frac{\partial w}{\partial y} + w \frac{\partial w}{\partial z} \right) = - \frac{\partial P}{\partial z} + \mu_{eff} \left(\frac{\partial^2 w}{\partial x^2} + \frac{\partial^2 w}{\partial y^2} + \frac{\partial^2 w}{\partial z^2} \right) \\ \text{energy :} \\ \rho_f c_{pf} \left(u \frac{\partial T_f}{\partial x} + v \frac{\partial T_f}{\partial y} + w \frac{\partial T_f}{\partial z} \right) = K_{eff} \left(\frac{\partial^2 T_f}{\partial x^2} + \frac{\partial^2 T_f}{\partial y^2} + \frac{\partial^2 T_f}{\partial z^2} \right) \end{array} \right. \quad (1)$$

where u , v , and w are the velocities of the fluid in the x , y , and z directions, respectively, ρ_f is the density of the fluid, P is the pressure of the fluid, μ_{eff} is the effective viscosity of the fluid, c_{pf} represents the constant-pressure specific heat capacity of the fluid, T_f is the temperature of the fluid, and K_{eff} is the thermal conductivity of the fluid. The viscosity and thermal conductivity of the fluid are expressed as

$$\mu_{eff} = \mu_f + \mu_t \quad (2)$$

$$K_{eff} = K_f + \frac{c_{pf}\mu_t}{Pr_t} \quad (3)$$

where μ_f is the dynamic viscosity of the fluid, μ_t is the turbulent dynamic viscosity of the fluid, K_f represents the thermal conductivity of the fluid, and Pr_t represents the Prandtl number of the fluid. The turbulent dynamic viscosity can be calculated using the density of the fluid (ρ_f), and the relationship between the turbulent kinetic energy dissipation rate (ε) and turbulent kinetic energy (k) is expressed as follows:

$$\mu_t = \frac{0.09\rho_f k^2}{\varepsilon} \quad (4)$$

The standard $k-\varepsilon$ model with turbulent kinetic energy and dissipation rate is adopted as follows:

$$\frac{\partial}{\partial x_i} (\rho_f k u_i) = \frac{\partial}{\partial x_j} \left[\left(\mu_f + \frac{\mu_t}{Pr_k} \right) \frac{\partial k}{\partial x_j} \right] + G - \rho_f \varepsilon \quad (5)$$

$$\frac{\partial}{\partial x_i} (\rho_f \varepsilon u_i) = \frac{\partial}{\partial x_j} \left[\left(\mu_f + \frac{\mu_t}{Pr_e} \right) \frac{\partial \varepsilon}{\partial x_j} \right] + C_1 \frac{\varepsilon}{k} G - C_2 \rho_f \frac{\varepsilon^2}{k} \quad (6)$$

where G is the turbulent kinetic energy caused by the average velocity gradient, Pr_k and Pr_e are the turbulent Prandtl numbers of the k and ε equations, respectively. Pr_k takes a value of 1, and Pr_e takes 1.3. C_1 and C_2 are constants, the value of C_2 is 1.92, and the value of C_1 is 1.44. In the above formulas, G can be calculated as follows:

$$G = \mu_t \left(\frac{\partial u_i}{\partial x_i} + \frac{\partial u_j}{\partial x_j} \right) \frac{\partial u_i}{\partial x_j} \quad (7)$$

In addition, a heat transfer model of the solid region of the electric motor must be considered. The energy conservation equation of the solid part of the electric motor is expressed as follows:

$$k_s \left(\frac{\partial^2 T_s}{\partial x^2} + \frac{\partial^2 T_s}{\partial y^2} + \frac{\partial^2 T_s}{\partial z^2} \right) + q = 0 \quad (8)$$

where k_s is the thermal conductivity of the solid material, T_s is the temperature of the solid region, and q is the calorific value per unit volume of the solid part. The calorific value originates from the heat loss in the motor, which is caused by various losses in the operation of the motor as displayed in [Table 2](#).

The heat source includes the stator core and winding part. In the

Table 4
Boundary conditions of the water-cooled motor.

Boundary condition	Value
Ambient temperature (K)	295
Ambient pressure (Pa)	101,325
Cooling water inlet temperature (K)	295
Cooling water inlet velocity (m/s)	0.1/0.3/0.5/0.7/0.9
Shell convection heat transfer coefficient (W/(m ² ·K))	5/10/15/20/25
Cooling water outlet pressure (Pa)	101,325

simulation process of the air-and water-cooled motors, the volume of the stator core and the winding are guaranteed to be the same. The total heat generation of the two cooling modes is the same, which is convenient for comparing the cooling effects of the different cooling methods.

2.3. Boundary Conditions

To solve the governing equations in the fluid and solid regions, the model must be set with the corresponding boundary conditions. For the air-cooled motor, the speed of the fan and the CHTC of the shell are considered the research objects. The influence of different speeds and the CHTCs on the cooling effect of the air-cooled motor is analyzed.

In an air-cooled motor, cold air is sucked from the upper end of the motor by a fan. The cold air passes through the gas channel between the stator core and winding, exchanges heat with the heat source and flows out from the lower part of the motor. In addition, to consider the influence of the rotating parts of the motor on the internal flow field and heat transfer performance, we must set the shell, permanent magnets, filter, and fan to the rotating mode. The rotational speed is the same as the fan speed, and the other parts remain stationary. The boundary conditions of the air-cooled motor are listed in Table 3.

The initial temperature of the motor is 295 K, and the pressure is 101,325 Pa. The motor shell is set as the convective heat transfer boundary condition. Assuming that the motor shell is heat exchange with the environment, the Robin boundary condition is adopted in thermodynamics [22]. The heat transfer between the motor housing and the environment is expressed as:

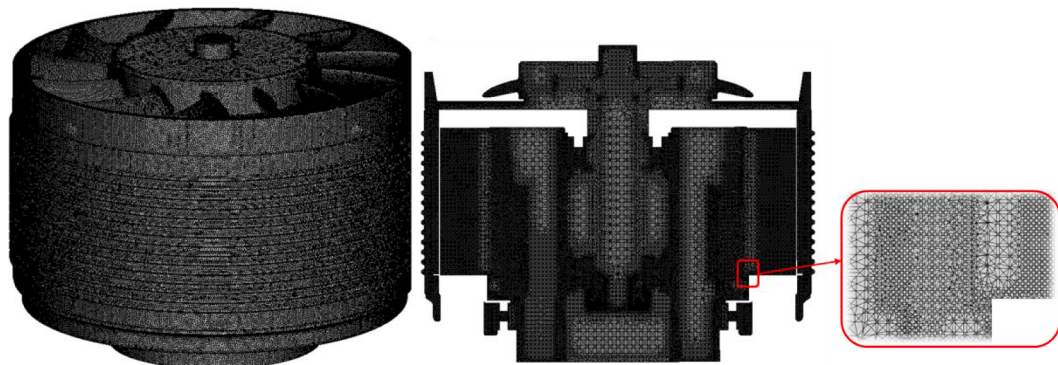
$$-k_{shell} \frac{\partial T_{shell}}{\partial n} = h_{shell-am} (T_{shell,out} - T_{am}) \quad (9)$$

where T_{shell} is the temperature distribution of the motor shell, $T_{shell,out}$ is the temperature at the outer surface of the shell, k_{shell} is the thermal conductivity of the motor shell, and $h_{shell-am}$ is the CHTC between the shell and environment. The n -direction indicates outward along the radial direction of the motor. The CHTC can be set to 5–25 W/(m²·K) according to the flight altitude and velocity of the UAV [23], and the specific values are listed in Table 3.

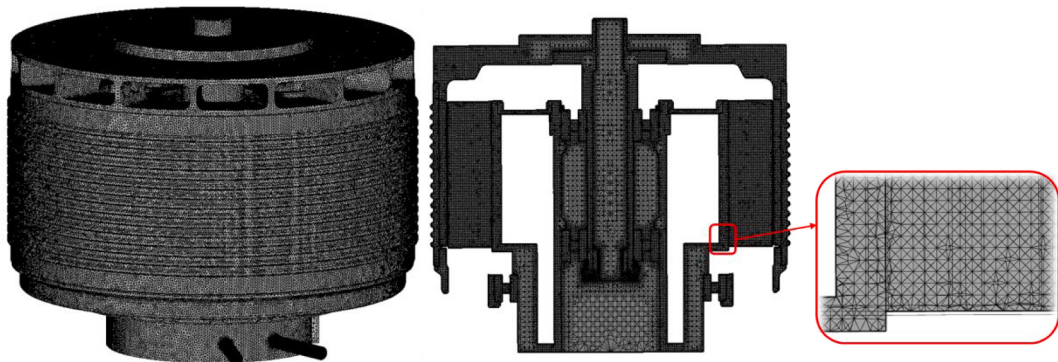
At the interface between the fluid and solid, the velocity is a no-slip boundary condition, and the heat flux conditions as follows:

$$\begin{cases} u_{interface} = v_{interface} = w_{interface} = 0 \\ -k_f \frac{\partial T_f}{\partial n} |_{interface} = -k_s \frac{\partial T_s}{\partial n} |_{interface} \\ T_{f,interface} = T_{s,interface} \end{cases} \quad (10)$$

where $u_{interface}$, $v_{interface}$ and $w_{interface}$ are the velocity component at the interface. Since it is a no-slip wall boundary, $u_{interface}$, $v_{interface}$ and $w_{interface}$ are equal to zero. Secondly, the heat flux on both sides of the interface should be consistent, that is, the heat flux calculated by Fourier's law is equal. At the same time, the heat transfer temperature difference between the fluid and the solid is ignored in the calculation of heat transfer, so that the temperature of the fluid side and the solid side



(a) Grid for the air-cooled motor



(b) Grid for the water-cooled motor

Fig. 4. Schematic of the unstructured grid for the air- and water-cooled motors (From left to right: the motor grid, the mid section grid and the grid near the wall).

Table 5

Grid independence test of air-cooled motor model.

Number of grids	Grid size (m^3)		Winding temperature (K)		Deviation from average temperature (K)	
	Maximum	Minimum	Maximum	Minimum	Maximum (Average value is 351.57 K)	Minimum (Average value is 348.43 K)
21,399,417	3.13×10^{-7}	4.66×10^{-13}	352.33	348.58	0.76	0.15
27,653,015	1.67×10^{-7}	4.35×10^{-13}	352.63	349.91	1.06	1.48
29,501,059	1.23×10^{-7}	3.17×10^{-13}	350.45	347.76	-1.12	-0.67
31,609,171	8.82×10^{-8}	1.87×10^{-13}	351.70	348.88	0.13	0.45
33,047,467	8.69×10^{-8}	1.22×10^{-13}	351.62	347.54	0.05	-0.89
34,447,747	7.18×10^{-8}	1.09×10^{-13}	350.28	347.52	-1.29	-0.91
40,167,489	6.17×10^{-8}	7.35×10^{-14}	351.95	348.79	0.38	0.36

Table 6

Grid independence test of water-cooled motor model.

Number of grids	Grid size (m^3)		Winding temperature (K)		Deviation from average temperature (K)	
	Maximum	Minimum	Maximum	Minimum	Maximum (Average value is 335.92 K)	Minimum (Average value is 329.01 K)
13,920,635	1.78×10^{-7}	5.26×10^{-13}	337.28	329.31	1.36	0.30
15,019,930	1.32×10^{-7}	3.95×10^{-13}	337.02	330.42	1.10	1.41
17,441,695	1.20×10^{-7}	3.77×10^{-13}	336.72	329.58	0.80	0.57
19,027,829	1.00×10^{-7}	2.65×10^{-13}	335.80	329.62	-0.12	0.61
21,278,887	8.26×10^{-8}	2.58×10^{-13}	335.04	328.47	-0.88	-0.54
23,996,142	8.17×10^{-8}	1.95×10^{-13}	334.00	328.12	-1.92	-0.89
25,966,045	6.21×10^{-8}	1.65×10^{-13}	335.58	327.58	1.66	-1.43

at the interface is equal.

The flow direction of the cooling water in the water-cooled motor is shown in Fig. 2 (c). The cooling water enters the cooling water channel from the inlet boundary at the lower end of the motor and flows around the circumference of the motor. After the water cools the motor, the temperature of the water increases and flows out from the outlet boundary. As with the air-cooled motor, the shell and permanent magnets of the motor are set as a rotating model, the speed is fixed at 800 rpm, and the other components remain stationary. The boundary conditions of the water-cooled motor are presented in Table 4.

The initial calculation conditions of the water-cooled motor are the same as those of the air-cooled motor, with an initial temperature of 295 K and pressure of 101,325 Pa. The inlet cooling-water temperature is maintained at 295 K, the cooling-water outlet is the pressure outlet, and the outlet pressure is the same as the atmospheric pressure. Eqs. (9) and (10) are also applicable to the boundary calculation of a water-cooled motor.

2.4. Simulation Settings

In this paper, according to the designed motor model, the unstructured grid is divided by ICEM software, and then the divided grid is imported into FLUENT for calculation condition setting and simulation calculation. Finally, the calculation results are imported into TECPLT for post-processing.

This section mainly introduces the simulation settings in FLUENT. The semi-implicit method for pressure-linked equations (SIMPLE) algorithm and finite volume method were adopted. The temperature distribution profile of the motor was obtained by solving the three control equations. Among them, the viscosity model used in the simulation is the standard $k-\epsilon$ model. The standard turbulence model is the main tool for engineering calculation, which has wide application scope, economy and reasonable accuracy. Eqs. (5)–(6) are the turbulent kinetic energy and dissipation rate equations to be solved by the standard $k-\epsilon$ model in this problem. In order to simulate the flow near the solid wall, it is necessary to study the consistency of the flow field and the algorithm. For this reason, the dimensionless coefficient $y +$ is proposed, and its calculation method is expression as [24].

$$y + = \frac{\Delta y u_t}{\nu} \quad (11)$$

where Δy is the distance from the nearest mesh point to the wall, u_t stands for the shear stress velocity and ν is kinematic viscosity. The wall treatment method used in this work is the enhanced wall method, which is not sensitive to the value of $y +$ [25]. Previous relevant literature has proved that in the enhanced wall method, even when the $y +$ value is between 3 and 10, the velocity and temperature profiles near the wall can still be reasonably displayed [26]. In the simulation of this work, because the model is specific, the size of the wall grid structure processed at different parts is different, and the $y +$ value in most areas is less than 1. However, there are still a small part's $y +$ value is large. For example, the maximum $y +$ value in air-cooled motor is 3.81, and the maximum $y +$ value in water-cooled motor is 4.21, which has little impact on the energy exchange in this work [26].

In addition, the simulation used a steady state algorithm based on pressure, and a single model uses 56 cores for parallel calculation, which takes about one to two days. In the spatial discrete model, the standard model is used for pressure, and the second-order upwind scheme is used for momentum and energy discretization.

In addition, because some components of the motor rotate during operation, it needs to be set separately. In the water-cooled motor, the rotating parts include the central shaft, shell, permanent magnets and filter. In the air-cooled motor, the rotating parts also include a fan. In order to simulate the effect of rotating structure on the surrounding fluid in the steady-state solver, the Multiple Reference Frame (MRF) method is adopted [27]. In the MRF method, the direction and speed of rotation need to be set for the rotating region. In this work, the rotation speed is the rotational speed of the motor, which is 800, 1200, 1600 and 2000 rpm respectively, and the rotation direction is the clockwise direction of the x -axis. In addition, it also needs to set the wall surfaces of the rotation area as rotating walls, and the rotation direction and speed are the same as the rotation area.

To ensure the accuracy of the calculation results, we set the residuals of the continuity variance and momentum equations to 10^{-4} and the residuals of the energy equations to 10^{-6} . The results were output after the calculated residuals converged.

3. Mesh Independence Test

A schematic of the grid structure of the air- and water-cooled motors is shown in Fig. 4. To stabilize the flow state of the cooling water at the

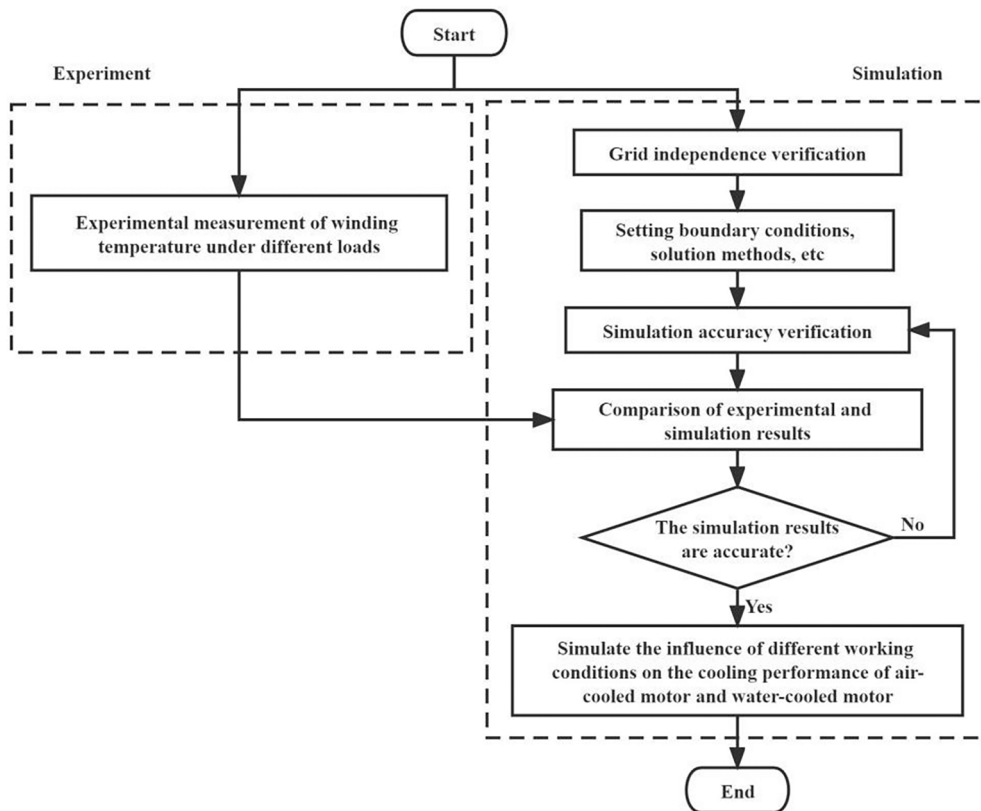


Fig. 5. Workflow diagram.

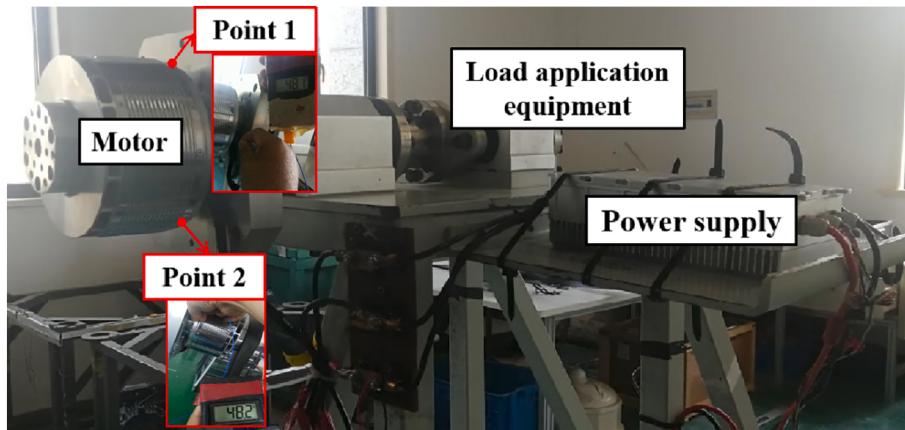


Fig. 6. Experimental test device.

Table 7
Physical properties of copper and aluminum.

Parameter	Copper	Aluminum
Density (kg/m^3)	8978	2719
Thermal conductivity ($\text{W}/(\text{m}\cdot\text{K})$)	387.6	202.4
Specific heat capacity ($\text{J}/(\text{kg}\cdot\text{K})$)	381	871

inlet and outlet boundaries and eliminate the influence of the boundary effects on the water-cooled motor, we slightly extended the grid area at the inlet and outlet boundaries of the cooling water. All grids adopt unstructured grids, and the specific size information is listed in Table 5 and Table 6. In addition, for the mesh of fluid area, due to the complex shape of the model, the method of densifying the overall mesh of fluid

Table 8
Temperature of the motor winding under different loads.

Working load (kg)	Point 1 (K)	Point 2 (K)	Average temperature (K)
0	318.0	318.0	318.0
20	321.2	321.1	321.15
40	337.9	343.5	340.7
60	380.7	372.2	376.45

area is adopted to ensure the calculation accuracy of fluid area.

After dividing the mesh, we verified the mesh independence of the model to avoid large errors caused by the number of meshes. The model of air- and water-cooled motor is divided by using unstructured grids of different sizes [28,29]. Each type of motor is divided into seven models

Table 9
Boundary conditions of the verified model.

Boundary condition	Value
Ambient temperature (K)	295
Ambient pressure (Pa)	101,325
Shell convection heat transfer coefficient ($\text{W}/(\text{m}^2 \cdot \text{K})$)	15
Working load (kg)	0/20/40/60

with different grid numbers. The temperature distribution in the motor is calculated using the boundary conditions and settings described in sections 2.3 and 2.4. For the air-cooled motor, the working load was 60 kg, the fan speed was 800 rpm, and the CHTC between the shell and environment was $15 \text{ W}/(\text{m}^2 \cdot \text{K})$. The results for the different mesh numbers are listed in Table 5.

For the water-cooled motor, the working load was 60 kg, the inlet velocity was 0.1 m/s , and the CHTC was $15 \text{ W}/(\text{m}^2 \cdot \text{K})$. The simulation results for the different mesh numbers are listed in Table 6.

It can be seen from the Table 5 and Table 6 that the temperature of motor winding is basically the same under different grids. In the air-cooled motor, the maximum difference between the highest temperature and the lowest temperature is 2.05 K and 2.39 K respectively. In water-cooled motors, the maximum difference of the highest temperature is 3.28 K, while the maximum difference of the lowest temperature is 2.84 K. The error between calculation results do not exceed 1% of the temperature, this shows that the number of grids has little influence on the calculation results, and proves the independence between grids. At the same time, we compared the difference between the calculation results and the average value of different grids. Considering the calculation accuracy and efficiency, we selected the model with 31,609,171 grids in the air-cooled motor and 19,027,829 grids in the water-cooled motor for calculation.

4. Experiment Test

4.1. Experimental Apparatus

Fig. 5 is the workflow diagram of this article. In this paper, the heat dissipation of the motor is studied by experiment and simulation. Among them, the experiment part is mainly to determine whether the conditions set in the simulation work are appropriate to ensure the rationality of the

simulation results. After verifying that the error between the model results and the test results is within the acceptable range, the simulation method can be used to study the influence of different fan speed, cooling water speed and CHTC on the heat dissipation capacity of the motor.

Fig. 6 shows the experimental test device used in this study. The ambient temperature during the experiments was 295 K. In the test method, a 300 V direct current was connected to the input port of the motor, and then the motor was applied with loads of 0, 20, 40, and 60 kg. Subsequently, the motor was started to run for a period, and when the motor operation state was stable, a temperature measuring instrument was used to measure the temperature of the two symmetrical points on the motor winding. When the operating temperature of the temperature measuring instrument is within the range of 273.15 to 773.15 K, the measurement uncertainty is $\pm (0.75\% + 1 \text{ K})$. The physical parameters of copper and aluminum are depicted in Table 7, and the experimental results are listed in Table 8.

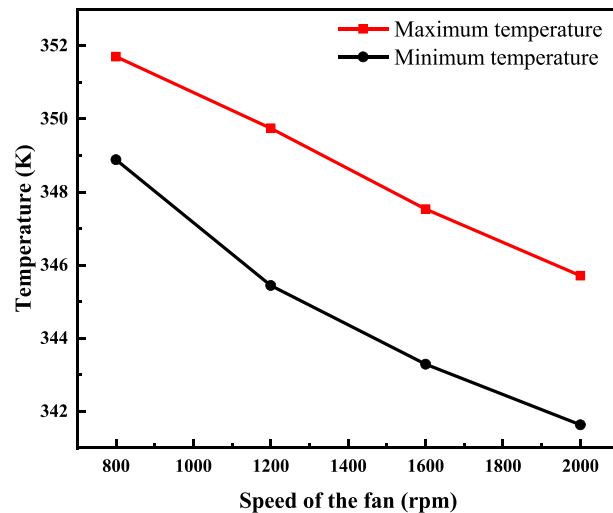


Fig. 8. Air-cooled motor winding temperature at different fan speeds.

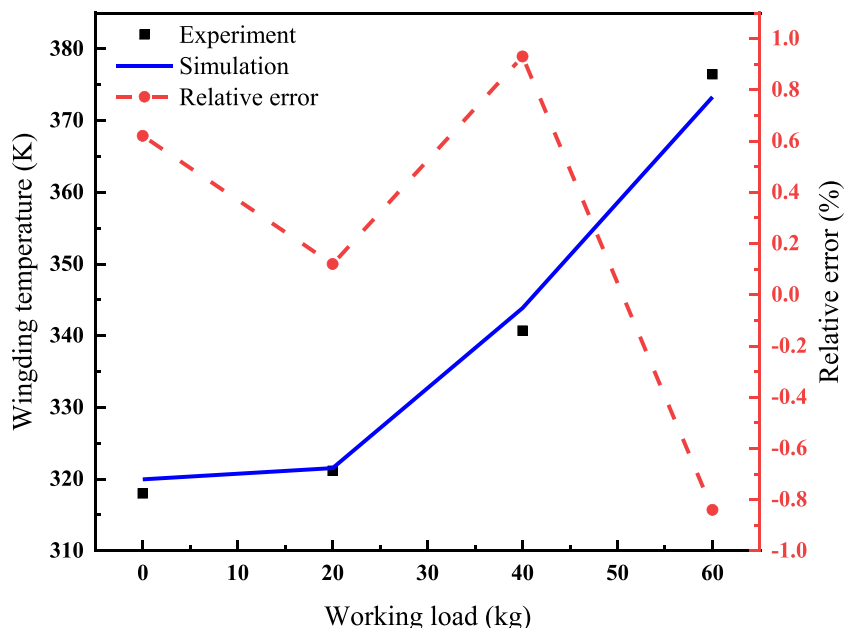


Fig. 7. Winding temperature obtained by experiment and simulation and their relative error.

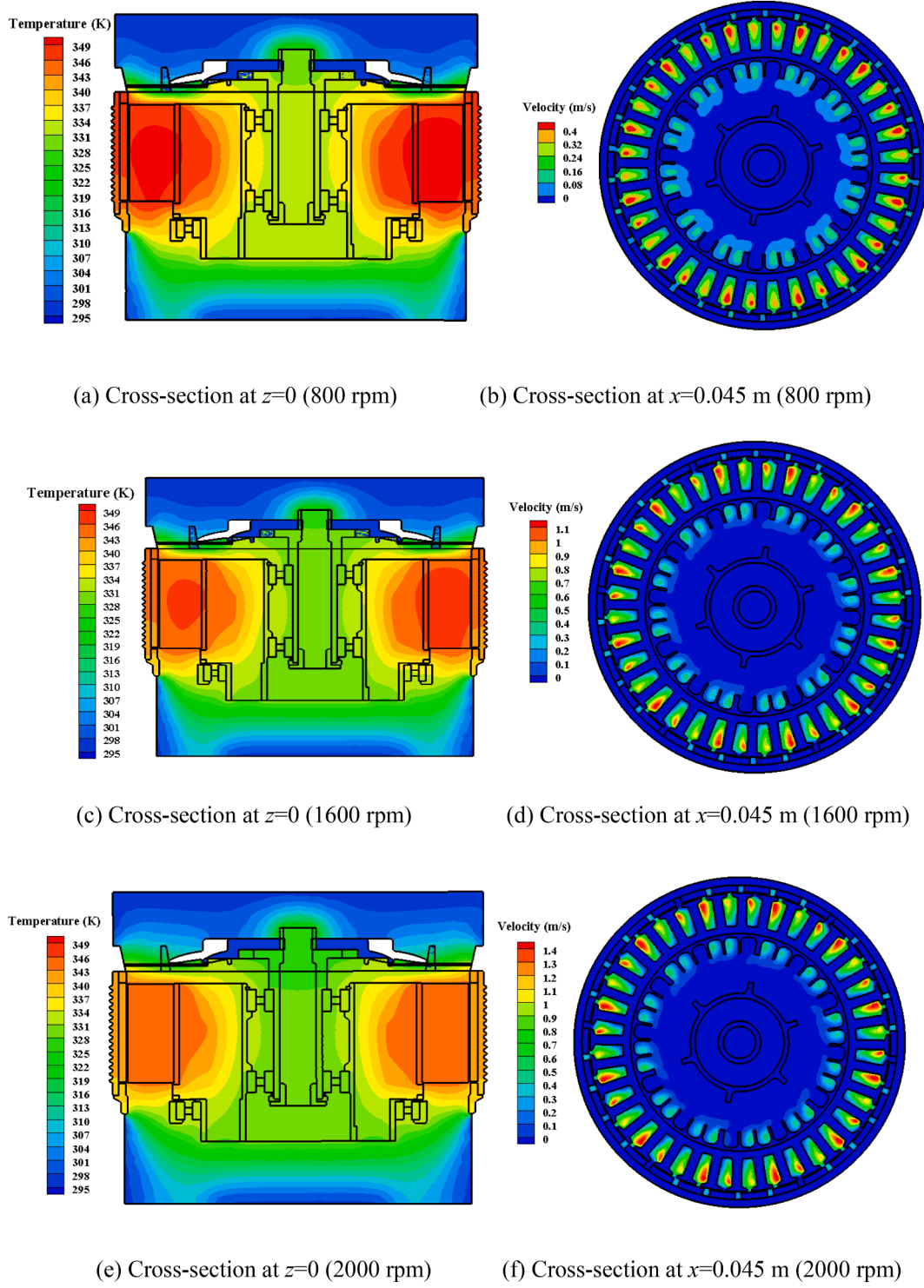


Fig. 9. Temperature and speed distribution of the air-cooled motor at different fan speeds.

4.2. Validation of the Simulation Model

In the validation model, we adopted the same settings as the test conditions, including ambient temperature, ambient pressure, motor speed, etc. See Table 9 for specific values. At the same time, the convection heat transfer coefficient of the outer wall is determined according to the engineering experience, assuming a constant value of 15 W/(m²·K). No cooling devices are included in the validation model. When the load of the motor is 0, 20, 40 and 60 kg respectively, the speed of the motor is 1180, 950, 1308 and 1600 rpm, respectively. Among

them, the speed of the motor can be regulated by an electronic speed control.

The temperature distribution of the motor was calculated using the simulation model and was compared to the experimental results with loads of 0, 20, 40, and 60 kg as shown in Fig. 7.

From the comparison between the experimental results and the simulation results, it can be found that the winding temperatures obtained by the two methods are basically the same. At the same time, Fig. 7 also shows the relative error between the experimental and simulation results, with the maximum error not exceeding 1%. This

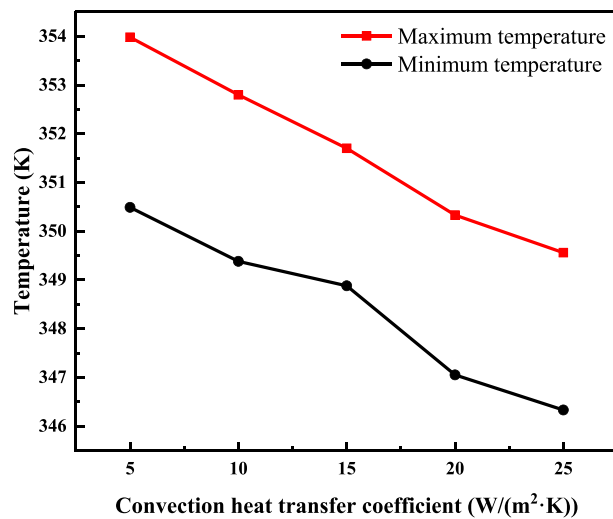


Fig. 10. Air-cooled motor winding temperature with different convection heat transfer coefficients.

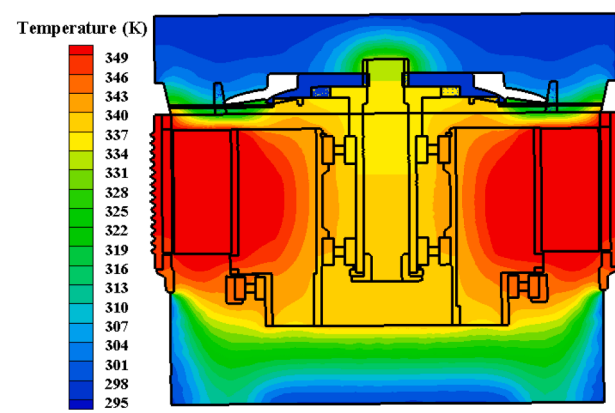
shows that the simulation result of motor temperature is reliable, and the model can be used to simulate the heat dissipation of motor. At the same time, the reasons for the difference between the simulation results and the experimental results are analyzed. First, different from the constant environmental conditions that can be maintained in the simulation, the environmental conditions will fluctuate during the experiment. At the same time, due to unstable power supply voltage and other reasons, the heating capacity of the motor may change, resulting in differences from the simulation. In addition, there will also be some random errors and systematic errors in the temperature measurement process. These will lead to differences between the results.

5. Results and Discussion

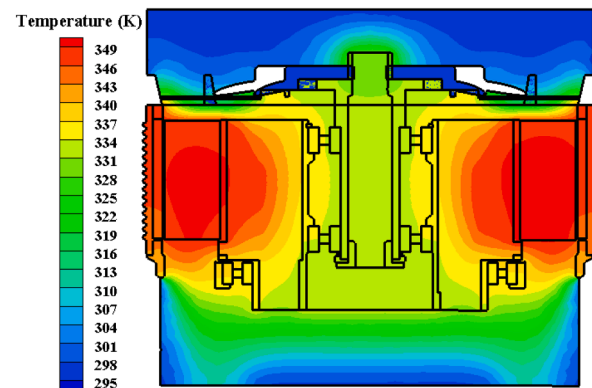
5.1. Fan Speed for the Air-Cooled Motor

The initial temperature of the motor was 295 K, the CHTC between the motor shell and environment was 15 W/(m²·K), and the motor load was 60 kg. The temperature field distributions of the motor at four fan speeds (800 rpm, 1200 rpm, 1600 rpm, and 2000 rpm) were obtained. The maximum and minimum temperature changes in the motor winding at different fan speeds are shown in Fig. 8. The maximum and minimum temperatures of the air-cooled motor decreased with increasing fan speed. Compared with the temperature of the motor shown in Fig. 7 without any cooling device, the air-cooled motor reduced the temperature of the motor to a certain extent. For example, when the load was 60 kg, the motor winding temperature without any cooling device was 373.3 K. When the fan speed was 800 rpm, the maximum temperature of the motor winding was 351.7 K, which was approximately 21.6 K lower than that of the motor without cooling device, which meant that the temperature increase decreased by 27.59%. As the fan speed increased, the temperature of the winding in the motor gradually decreased. When the fan speed increased from 800 to 2000 rpm, the maximum temperature of the motor decreased by 6 K, and the cooling efficiency increased by 27.78%. This was because, as the fan speed increased, the airflow velocity in the cooling channel of the air-cooled motor gradually increased. When the airflow velocity increased, the flow rate of cold air passing through the motor increased, thereby increasing the CHTC between the cold air and motor. This ultimately reduced the temperature of the motor.

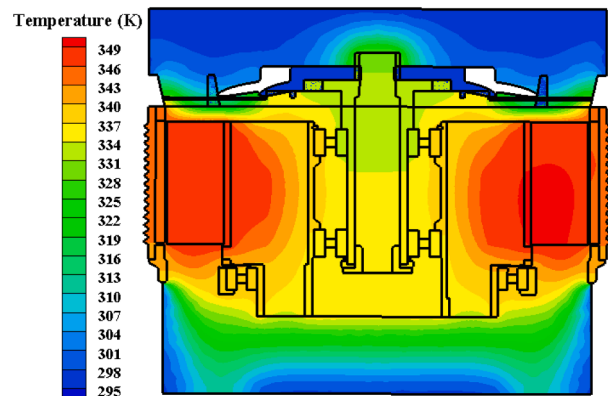
The temperature distribution of the motor on the $z = 0$ plane at 800, 1600, and 2000 rpm was intercepted (Fig. 9 (a), (c) and (e)). The maximum temperature in the motor winding, as well as the high-



(a) Cross-section in the $z=0$ (5 W/(m²·K)))



(b) Cross-section in the $z=0$ (15 W/(m²·K)))



(c) Cross-section in the $z=0$ (25 W/(m²·K)))

Fig. 11. Air-cooled motor temperature distribution for different convection heat transfer coefficients.

temperature area in the motor, decreased with an increase in the rotational speed of the fan. This was due to the increased pressure differential across the fan as the fan speed increased, resulting in a greater inlet airflow velocity. The speed profiles in Fig. 9 (b), (d), and (f) show that the speed of the air flowing through the motor increased with the speed of the fan. The CHTC increased when the airflow velocity increased. This meant that the cooling efficiency of the motor can be improved by increasing the fan speed to increase the flow of cold air

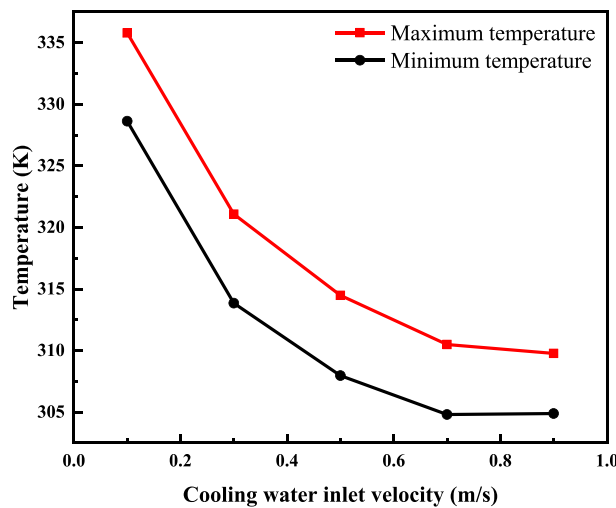


Fig. 12. Water-cooled motor winding temperature with inlet velocities.

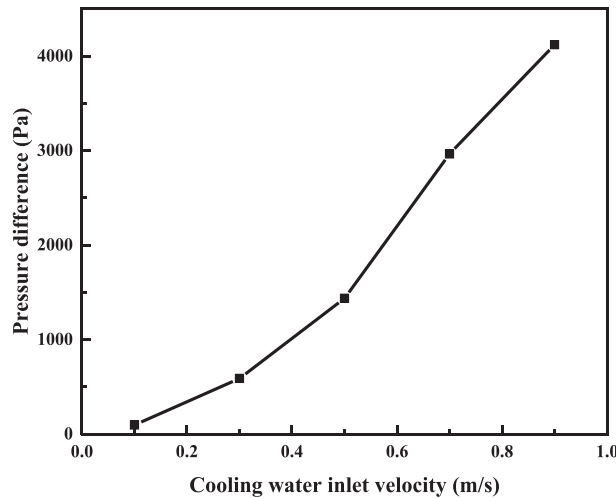


Fig. 13. Differential pressure of cooling water with inlet velocities.

through the motor.

5.2. Convection Heat Transfer Coefficient of an Air-Cooled Motor

The CHTCs between the motor shell and environment were set to 5, 10, 15, 20, and 25 W/(m²·K), and the ambient temperature was 295 K. The speed of the motor was 800 rpm and the load was fixed at 60 kg. The influence of the different CHTCs on the motor winding temperature is shown in Fig. 10. Both the maximum and minimum temperatures in the winding decreased with an increase in the external CHTC. This was because, as the CHTC of the ambient convection increased, the motor could dissipate more heat through the shell, thereby reducing the temperature of the heat source. When the CHTC increased from 5 to 25 W/(m²·K), the maximum temperature of the winding decreased by 4.43 K, and the cooling efficiency increased by 22.93%. Different convection heat transfer coefficients have influence on the temperature distribution of air-cooled motor. It can be seen from the temperature cloud diagram in Fig. 10 that with the increase of the convection heat transfer coefficient, the area where the temperature is higher than 349 K on the section is decreasing. At the same time, because the convective heat transfer coefficient selected in the study is small, the heat dissipation power through convective heat transfer is small, so the influence of the convective heat transfer coefficient on temperature is limited.

Fig. 11 (a), (b), and (c) show the cross-sectional temperature

distribution of the motor when the CHTCs were 5, 15, and 25 W/(m²·K), respectively. It can be seen that when CHTC is 5 W/(m²·K), the temperature in the winding and stator area of the motor in the section exceeds 349 K. However, with the increase of CHTC, the area of the area where the temperature exceeds 349 K is shrinking. When the CHTC increases to 25 W/(m²·K), only the temperature of some areas in the right winding area exceeds 349 K. This shows that although the CHTC has no significant impact on the maximum temperature of the motor, increasing the CHTC can still improve the cooling efficiency of the motor to a certain extent and reduce the area of the high-temperature area.

5.3. Inlet Flow Rate for Water-Cooled Motors

The inlet flow velocities were set as 0.1, 0.3, 0.5, 0.7, and 0.9 m/s. The load was set at 60 kg, the initial temperature of the motor and cooling water was set, and the ambient temperature was 295 K. The CHTC between the motor shell and environment was set as 15 W/(m²·K). The maximum and minimum temperatures of the winding at different inlet flow velocities were determined as shown in Fig. 12.

As the inlet flow rate increased, both the maximum and minimum temperatures of the motor winding decreased. When the motor does not have any cooling device, the maximum temperature of the winding in the motor is 373.3 K (78.3 K higher than ambient temperature). In water-cooled motors, when the cooling water inlet velocity is 0.1 m/s, the maximum temperature of the motor winding is 335.8 K (40.8 K higher than ambient temperature), which is 37.5 K lower than the motor without cooling device. That is to say, compared with the motor without cooling device, the temperature rise of water-cooled motor with inlet velocity of 0.1 m/s decreases by 47.89%. In addition, with an increase in the inlet flow velocity, the magnitude of the temperature decrease gradually decreased. When the inlet velocity reached 0.7 m/s, as the inlet flow velocity continued to increase, the maximum and minimum temperatures did not change, indicating that the cooling limit of the water-cooled motor was reached, and the cooling efficiency of the motor could not be strengthened by further increasing the inlet velocity of the cooling water. When the inlet velocity of the cooling water increased from 0.1 to 0.9 m/s, the maximum temperature of the motor winding decreased from 335.8 to 310.5 K. That is to say, when the inlet velocity of cooling water is 0.1 m/s, the maximum temperature of motor winding decreases by 37.5 K compared with that without cooling device, while when the inlet velocity is 0.9 m/s, the maximum temperature of motor winding can be reduced by another 25.3 K on this basis, and the cooling efficiency increased by 67.47%.

In addition, it should be noted that with the increase of the cooling water flow rate, the pressure difference between the inlet and outlet of the motor cooling water channel will also increase, as shown in Fig. 13. When the inlet speed of cooling water increases from 0.1 to 0.9 m/s, the pressure difference between the inlet and outlet of cooling water increases from 93.35 Pa to 4120.21 Pa. As the import and export pressure difference increases, the high pump power is required. Therefore, in order to obtain a better cooling effect, it is necessary to provide more power in the water-cooled motor. In practical applications, it is necessary to balance the relationship between heat dissipation capacity and pump power, and make choices according to the actual situation. For example, compared with the inlet speed of 0.7 m/s, the inlet speed of 0.9 m/s can only reduce the maximum temperature of the motor by 0.72 K, but it will consume about 39% higher pump work, which does not conform to the principle of economy.

Fig. 14 (a)–(f) show the temperature distributions of the motor and cooling water for different cooling water inlet flow velocities. The temperature distribution of the motor is represented by the cross-sectional temperature of the $z = 0$ plane (Fig. 14 (a), (c), and (e)). Area A represents the cooling water and area B represents the heat source. The temperature on the left side of the motor was slightly lower than that on the right side, which was related to the flow direction of the cooling water. The cooling water first entered from the inlet on the left

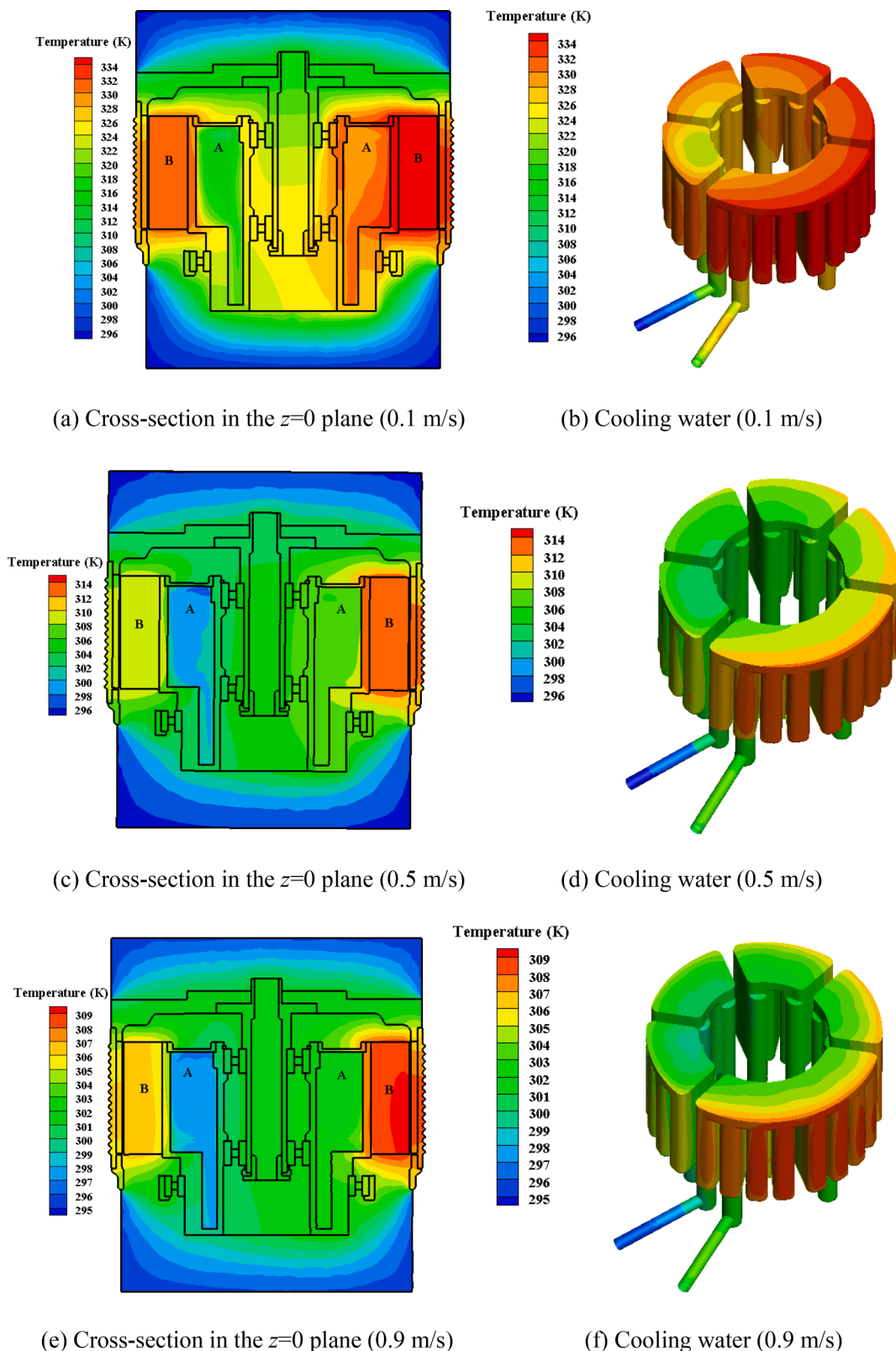


Fig. 14. Water-cooled motor temperature distribution for different cooling water inlet velocities.

side of the motor, flowed clockwise, and then flowed out from the outlet. Therefore, the temperature of the cooling water cooling the left side of the motor was lower and the cooling effect was greater. As the cooling water flowed clockwise, the temperature of the cooling water gradually increased because of the heat absorbed from the heat source, resulting in

a poor cooling effect. The temperature on the right side of the motor was higher than that on the left side of the motor. The change in the cooling water temperature is shown in Fig. 14 (b), (d), and (f), and the temperature of the cooling water increased continuously during the entire flow process. With an increase in the inlet velocity, the temperature

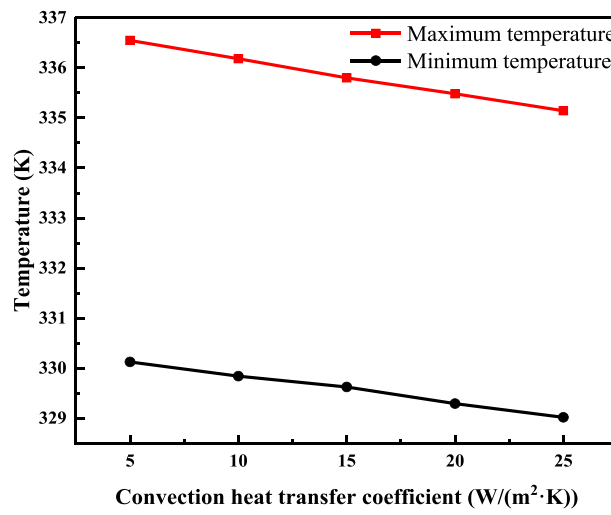


Fig. 15. Water-cooled motor winding temperature with convection heat transfer coefficients.

increase of the cooling water decreased, and the high-temperature area also decreased. This implied that an increase in the inlet flow velocity enhanced the heat dissipation effect of the water-cooled motor.

5.4. Convection Heat Transfer Coefficient of Water-Cooled Motor

The cooling effect of the motor was simulated under five conditions of the CHTCs with 5, 10, 15, 20, and 25 W/(m²·K). The simulated ambient temperature is 295 K, the inlet speed of cooling water is 0.1 m/s, and the working load of the motor is 60 kg. The maximum and minimum temperature changes in the motor winding are shown in **Fig. 15**. Increasing the CHTC also slightly reduced the highest temperature in the water-cooled motor; however, the reduction was not significant. When the CHTC increased from 5 to 25 W/(m²·K), the maximum temperature of the motor winding decreased by only 1.04 K, and the minimum temperature decreased by only 0.8 K. The cooling efficiency of the motor increased by only 2.77%. This was because the thermal conductivity and heat capacity of water was higher than those of air, and the convection heat transfer intensity between the motor and cooling water was significantly greater than the convection heat transfer intensity of the casing, resulting in most of the heat of the motor being absorbed and removed by the cooling water. The CHTC of the shell had minimal effect on the maximum and minimum temperatures in the water-cooled motor.

Fig. 16 (a), (c), and (e) show the temperature distribution of the motor section at $z = 0$ under different CHTCs. Area A is the cooling water, and area B is the heat source. **Fig. 16** (b), (d), and (f) show the temperature distribution of cooling water under different CHTCs. Although **Fig. 15** shows that the maximum and minimum temperatures in the motor winding were not significantly affected by the CHTC, we can observe from the cross-sectional temperature distribution that with the increase in the CHTC, the area of the high-temperature region in the motor gradually decreased. In addition, the temperature distribution of the cooling water in the motor varied with the increase in the CHTC. As the CHTC increased, the volume of the low temperature region in the cooling water also increased slightly. Although the change of the CHTC had a slight effect on the maximum and minimum temperature in the winding of the water-cooled motor, the increase in the CHTC reduced the proportion of the high temperature area in the water-cooled motor. Therefore, increasing the CHTC increased the cooling efficiency of the water-cooled motor to a certain extent.

5.5. Comprehensive Performance Comparison of the Air- and Water-Cooled Motors

On the UAV, due to the limited power that can be provided by the power supply, there are certain requirements for the weight of the UAV [30]. With the increase of UAV weight, the energy required to maintain flight is also increasing. In order to improve the endurance of the UAV, weight of UAV is usually taken as the optimization objective during structural design [31]. In addition, additional components are added to the motor in the air- and water-cooled method, which increases the weight of the UAV and additional heat dissipation power consumption. Compared with the increased mass, the power consumed by the increased heat sink has almost negligible impact on the UAV. Therefore, the heat dissipation efficiency and structure weight of the motor are taken as the influencing factors for evaluating the motor performance [32]:

$$F = \frac{M_{cool}}{M_{ori}} + \frac{T_{cool}}{T_{ori}} \quad (12)$$

where M_{ori} is the weight of the motor without any cooling device, M_{cool} is the weight of the air-cooled or water-cooled motor, T_{ori} is the temperature of the motor winding without any cooling device, and T_{cool} is the temperature of the motor winding after air or water cooling. The value of F is small, indicating that the motor with this cooling method has good heat dissipation performance and is lightweight; that is, the heat dissipation benefit introduced by increasing the weight of the motor is high.

The motor weight (M_{ori}), without any cooling device, was 3.682 kg. The air-cooled motor replaced the upper top cover with a fan, and its total weight was 3.692 kg. A water-cooled motor also must consider the weight of the cooling water. The total weight of the water-cooled motor was 4.367 kg. When the motor load was 60 kg, the temperature (T_{ori}) of the motor winding without a cooling device was 373.3 K. The values of the motor objective function for the different cooling methods are shown in **Fig. 17**.

The comprehensive performance evaluation factor of the air-cooled motor was significantly smaller than that of the water-cooled motor. In the water-cooled motor, the minimum value of F was 2.02, whereas the maximum F value of the air-cooled motor was only 1.94. This demonstrates that, although the cooling capacity of the air-cooled motor is smaller than that of the water-cooled motor, the weight requirement of the air-cooled motor is smaller than that of the water-cooled motor. If the cooling power requirement of the motor is not large but the weight requirement is very low, an air-cooled motor is the best option. If a higher cooling capacity can be obtained by sacrificing weight, a water-cooled motor can be selected.

This paper studies the difference of cooling capacity between air- and water-cooled motors. The influences of different fan speed, cooling water speed and convection heat transfer coefficient on the cooling performance are compared. For light UAV, the motor power is not large, but there are strict restrictions on the weight of UAV [33,34]. At this time, air-cooled motor can be used, and the fan speed can be adjusted to match the heating power of the motor. For some UAVs with large motor heating power and high temperature control requirements [35,36], water-cooled motor can be used to improve the cooling capacity by sacrificing weight. At the same time, increasing the speed of cooling water can also improve the cooling efficiency of water-cooled motors.

6. Conclusions

Two schemes, air cooling and water cooling, were designed for the heat dissipation of the motor in an unmanned aerial vehicle. The maximum temperature of the air-cooled motor decreased with increasing fan speed. When the fan speed was increased from 800 to 2000 rpm, the cooling capacity increased by 27.78%. The maximum temperature of the air-cooled motor decreased with an increase in

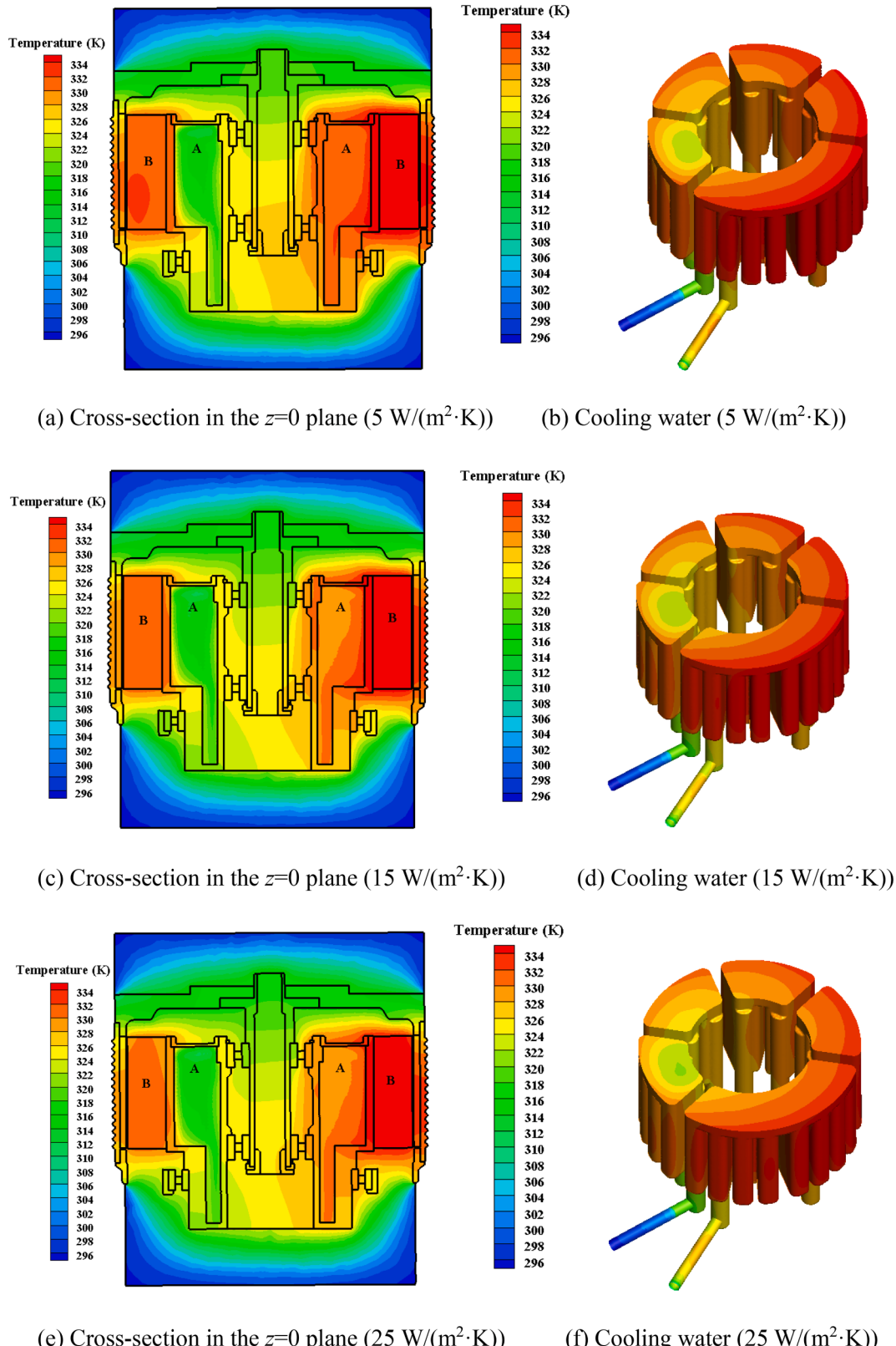


Fig. 16. Water-cooled motor temperature distribution for different convection heat transfer coefficients.

convection heat transfer coefficient. When the convection heat transfer coefficient increased from 5 to $25 \text{ W}/(\text{m}^2 \cdot \text{K})$, the maximum temperature of the motor winding decreased by 4.43 K, and the cooling capacity increased by 22.93%. The maximum temperature of the water-cooled motor decreased as the inlet speed of the cooling water increased.

When the inlet flow rate was 0.1 m/s , the maximum temperature of the motor winding was 335.8 K , which was significantly lower than that of the air-cooled motor. Compared with the motor without cooling, the temperature increase decreased by 47.89%. When the inlet flow rate increased from 0.1 to 0.9 m/s , the maximum temperature of the winding

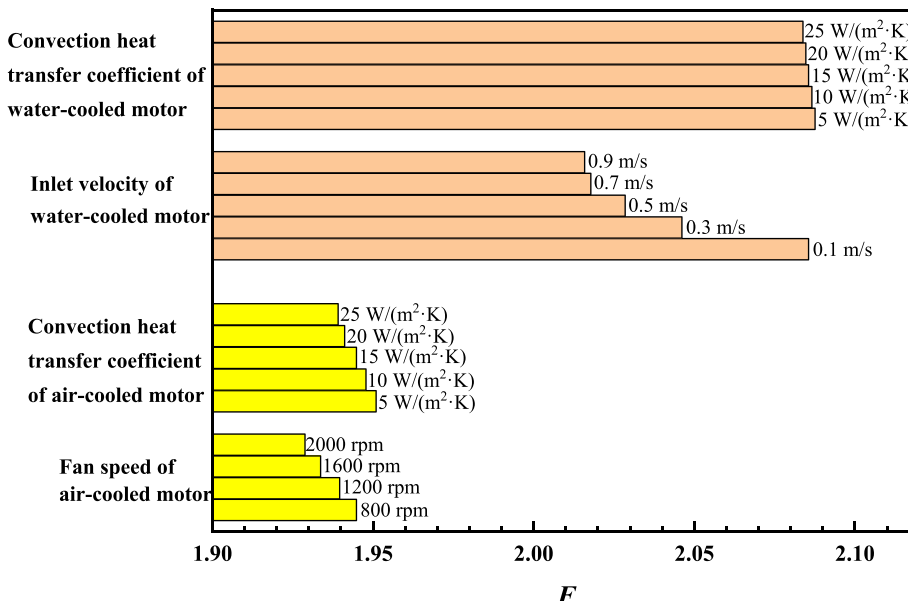


Fig. 17. Comprehensive performance evaluation factor for different cooling methods.

decreased by 25.3 K, and the cooling capacity increased by 67.47%. When the velocity of cooling water was 0.7 m/s, the comprehensive performance of the water-cooled motor reached the highest level. Increasing the convection heat transfer coefficient slightly reduced the highest temperature in the water-cooled motor; however, the reduction was not significant. When the convection heat transfer coefficient increased from 5 to 25 W/(m²·K), the maximum temperature of the winding decreased by 1.04 K, and the cooling capacity only increased by 2.77%. A comprehensive performance evaluation factor is proposed to determine the condition that uses an air-cooled motor or a water-cooled motor. The research in this paper can provide some guidance for the motor design on UAV in the future.

CRediT authorship contribution statement

Min Chang: Methodology, Validation, Formal analysis, Investigation, Writing – original draft. **Bingzhu Lai:** Methodology, Validation, Formal analysis, Investigation, Writing – original draft. **Hui Wang:** Writing – review & editing, Formal analysis, Supervision. **Junqiang Bai:** Writing – review & editing. **Zhaoyong Mao:** Writing – review & editing.

Declaration of Competing Interest

None.

Data availability

Data will be made available on request.

Acknowledgments

This work was supported by the China Postdoctoral Science Foundation (No. 2021M692632 and No. 2022T15532).

References

- [1] Z. Wang, J. Zhou, G. Rizzoni, A review of architectures and control strategies of dual-motor coupling powertrain systems for battery electric vehicles, *Renew. Sust. Energ. Rev.* 162 (2022), 112455.
- [2] M.L.D. Klerk, A.K. Saha, Performance analysis of DTC-SVM in a complete traction motor control mechanism for a battery electric vehicle, *Heliyon* 8 (4) (2022), e09265.
- [3] H. Zhou, Y. Wan, H. Ye, M. Jiang, J. Wang, Real-time energy-efficient optimal control of high-speed electric train, *Control. Eng. Pract.* 112 (2021), 104825.
- [4] X. Li, K. Sun, F. Li, General optimal design of solar-powered unmanned aerial vehicle for priority considering propulsion system, *Chin. J. Aeronaut.* 33 (8) (2020) 2176–2188.
- [5] Y. Xu, W. Zhu, J. Li, L. Zhang, Improvement of endurance performance for high-altitude solar-powered airships: a review, *Acta Astronaut.* 167 (2020) 245–259.
- [6] N. Thapa, S. Ram, S. Kumar, J. Mehta, All electric aircraft: a reality on its way, *Mater. Today Proc.* 43 (2021) 175–182.
- [7] Y. Gai, M. Kimiaeigui, Y. Chong, J. Widmer, M. Popescu, X. Deng, Cooling of automotive traction motors: schemes, examples, and computation methods, *IEEE Trans. Ind. Electron.* 66 (3) (2019) 1681–1692.
- [8] B. Melka, J. Smolka, J. Hetmanczyk, P. Lasek, Numerical and experimental analysis of heat dissipation intensification from electric motor, *Energy* 182 (2019) 269–279.
- [9] C. Kim, K.S. Lee, S.J. Yook, Effect of air-gap fans on cooling of windings in a large-capacity, high-speed induction motor, *Appl. Therm. Eng.* 100 (2016) 658–667.
- [10] M. Kang, H. Wang, L. Guo, T. Shi, C. Xia, Self-circulation cooling structure design of permanent magnet machines for electric vehicle, *Appl. Therm. Eng.* 165 (2020), 114593.
- [11] S. Hyeon, C. Kim, K.S. Lee, Thermal enhancement of an air-cooled motor with a flow guide, *Int. J. Heat Mass Transf.* 183 (2022) 22228.
- [12] E. Galloni, P. Parisi, F. Marignetti, G. Volpe, CFD analyses of a radial fan for electric motor cooling, *Therm. Sci. Eng. Prog.* 8 (2018) 470–476.
- [13] Z. Pei, J. Zhao, J. Song, K. Zong, Z. He, Y. Zhou, Temperature field calculation and water-cooling structure design of coreless permanent magnet synchronous linear motor, *IEEE Trans. Ind. Electron.* 68 (2) (2021) 1065–1076.
- [14] H. Chiu, J. Jang, W. Yan, R.B. Shiao, Thermal performance analysis of a 30 kW switched reluctance motor, *Int. J. Heat Mass Transf.* 114 (2017) 145–154.
- [15] F. Han, H. Guo, X. Ding, Design and optimization of a liquid cooled heat sink for a motor inverter in electric vehicles, *Appl. Energy* 291 (2021), 116819.
- [16] B. Ge, J. Zhang, D. Tao, Temperature prediction and cooling structure optimization of explosion-proof high pressure water-cooled double speed motor, *Energy Rep.* 8 (2022) 3891–3901.
- [17] A. Nikbakht, H.R. Izadfar, M. Jazaeri, Classification and comparison of rotor temperature estimation methods of squirrel cage induction motors, *Measurement* 145 (2019) 779–802.
- [18] I. López, E. Ibarra, A. Matallana, J. Andreu, I. Kortabarria, Next generation electric drives for HEV/EV propulsion systems: technology, trends and challenges, *Renew. Sust. Energ. Rev.* 114 (2019), 109336.
- [19] J. Jang, H. Chiu, W. Yan, M.C. Tsai, P. Wang, Numerical study on electromagnetics and thermal cooling of a switched reluctance motor, case stud., *Therm. Eng.* 6 (2015) 16–27.
- [20] A.E.L. Hocine, S. Poncet, H. Fellouah, CFD modeling and optimization by metamodels of a squirrel cage fan using OpenFoam and Dakota: ventilation applications, *Build. Environ.* 205 (2021) 08145.
- [21] W. Yan, H. Teng, C. Li, M. Ghalambaz, Electromagnetic field analysis and cooling system design for high power switched reluctance motor, *Int. J. Numer. Methods Heat Fluid Flow* 29 (5) (2019) 1756–1785.
- [22] W. Chen, Y. Ju, D. Yan, L. Guo, Q. Geng, T. Shi, Design and optimization of dual-cycled cooling structure for fully-enclosed permanent magnet motor, *Appl. Therm. Eng.* 152 (2019) 338–349.
- [23] A.F. Mills, *Heat Transfer*, 2nd ed., Prentice-Hall, New York, 1999.

- [24] Y. Zhang, X. Zhang, Y. Li, M. Chang, J. Xu, Aerodynamic performance of a low-Reynolds UAV with leading-edge protuberances inspired by humpback whale flippers, Chin. J. Aeronaut. 34 (5) (2021) 415–424.
- [25] R. Cabello, A.E.P. Popescu, J.B. Ruiz, D.C. Cantarell, J. Llorens, Heat transfer in pipes with twisted tapes: CFD simulations and validation, Comput. Chem. Eng. 166 (2022), 107971.
- [26] A. Muhamad, Numerical analysis of friction factor for a fully developed turbulent flow using $k-\epsilon$ turbulence model with enhanced wall treatment, Beni-Suef U.J. Basic 3 (4) (2014) 269–277.
- [27] H. Ma, N. Cai, L. Cai, F. Si, Effects of the forced convection induced by assistant fans on the thermal performance of an indirect dry cooling system, Case Stud. Therm. Eng. 35 (2022), 102141.
- [28] I.B. Celik, U. Ghia, P.J. Roache, C.J. Freitas, Procedure for estimation and reporting of uncertainty due to discretization in CFD applications, J. Fluid Eng. Trans. ASME 130 (7) (2008), 078001.
- [29] P. Dubey, U. Ghia, L.A. Turkevich, Numerical investigation of sheath and aerosol flows in the flow combination section of a baron Fiber classifier, Aerosol Sci. Technol. 48 (8) (2014) 896–905.
- [30] X. Wang, B. Li, G. Gerad, K. Huang, I. Stone, S. Worrall, Y. Yan, A critical review on thermal management technologies for motors in electric cars, Appl. Therm. Eng. 201 (2022), 117758.
- [31] X. Li, K. Sun, F. Li, General optimal design of solar-powered unmanned aerial vehicle for priority considering propulsion system, Chin. J. Aeronaut. 33 (8) (2020) 2176–2188.
- [32] Y. Zhang, J. Peng, R. Yang, L. Yuan, S. Li, Weight and performance optimization of rectangular staggered fins heat exchangers for miniaturized hydraulic power units using genetic algorithm, Case Stud. Therm. Eng. 28 (2021), 101605.
- [33] M. Gadalla, S. Zafar, Analysis of a hydrogen fuel cell-PV power system for small UAV, Int. J. Hydrogen Energ. 41 (15) (2016) 6422–6432.
- [34] D. Sziroczak, D. Rohacs, J. Rohacs, Review of using small UAV based meteorological measurements for road weather management, Prog. Aerosp. Sci. 134 (2022), 100859.
- [35] H. Dong, L. Ruan, Y. Wang, J. Yang, F. Liu, S. Guo, Performance of air/spray cooling system for large-capacity and high-power-density motors, Appl. Therm. Eng. 192 (2021), 116925.
- [36] P. Fan, S. Huang, H. Wang, D. Luo, H. Li, M. Sun, Fundamental frequency region-based thermal control of power electronics modules in high power motor drive, Microelectron. Reliab. 88-90 (2018) 1242–1246.